AIAA JOURNAL
Vol. 39, No. 9, September 2001

Numerical Investigation of Strong Crossing Shock-Wave/ Turbulent Boundary-Layer Interactions

J. D. Schmisseur* and Datta V. Gaitonde†
U.S. Air Force Research Laboratory, Wright–Patterson Air Force Base, Ohio 45433-7521

Numerical results are reported for very strong fully separated three-dimensional crossing shock-wave/turbulent-boundary-layer interactions at Mach 5. The flowfield is generated by two sharp fins mounted at angle of attack on a flat plate in a manner closely resembling a portion of a scramjet inlet. Two symmetric configurations with fin angles of attack of 18 and 23 deg are considered. The flowfield is determined through solution of the full three-dimensional mean compressible Navier–Stokes equations using a sophisticated k–ϵ closure model. The computations are validated by comparison with available experimental data. The close similarity between the simulated and experimental surface oil flow patterns—particularly in the strong 23 × 23 case in which new topological patterns appear—indicate that the computations are successful in obtaining the mean flowfield. These additional features include not only new critical points but also phenomena associated with secondary separation. Ramifications of the new surface features on the off-surface flow are examined in great detail by probing the computed flowfield. Previous models of the flowfield evolution with interaction strength are updated to include these new features.

Introduction

ONE of the major obstacles to achieving sustained hypersonic flight is associated with difficulties in the design of efficient airbreathing propulsion systems. Scramjets comprise a key area of interest in this endeavor because, in principle, the large losses integral to high-speed ramjet operation can be minimized. Major problems persist, however, in the development of practical scramjet designs. For example, efficient combustion at high speed is predicated upon successful and rapid fuel-air mixing without excessive flow distortion.

One phenomenon, which generally degrades the flowfield quality in proposed scramjet designs, is that of shock-wave/turbulent boundary-layer interactions. Such interactions typically occur when a sidewall or compression surface oriented at angle to the incoming flow generates a shock wave, which then interacts with the turbulent boundary layer developing on an adjacent surface. The resultant effects are complicated and can include flow separation and generation of vortical structures. A number of review papers covering swept shock-wave/turbulent boundary-layer interactions are available (see, for example, Refs. 1 and 2).

The focus of the present study is a simulated inlet comprised of the double fin shown schematically in Fig. 1, where two fins are mounted on the flat plate at an angle of attack to the incoming flow. In recent years this canonical inlet configuration has been subjected to intense scrutiny. Particular emphasis has been placed on understanding both the physics of turbulent interactions and the fundamental aspects of separation. The starting point for the present analysis lies in the three-dimensional model proposed by Gaitonde et al. in a series of papers.[3–7] For strong (or fully separated) interactions the principal elements of the flow are described in terms of four flow regimes[3]: the separated boundary layer, vortex interaction, centerline vortices, and entrainment. Each regime has a distinct "footprint," and the lines of coalescence and divergence that mark the boundaries between the various regimes will be discussed in more detail in a later section.

In Ref. 5 the evolution of the flowfield with increasing interaction strength was described in terms of the topological bifurcations observed when the fin angles were increased from 7 × 7 to 15 × 15 at Mach 4. An elegant description of the evolution can be presented in terms of the appearance of critical points: at such locations the velocity vector is undefined and, when observed in surface flow visualization, the shear stress vanishes. The two primary types of critical points are saddles and nodes/foci. Reference 8 contains a classification of the various types of critical points, their significance, and the laws governing their behavior. In the strongest interactions examined in previous efforts, the final stage of evolution consists of four critical points on the plate, with two nodes N^1 and N^2 on the centerline and two saddles (S^1 and its mirror image on the other side of the plane of symmetry), arranged in a diamond-shaped pattern.[5]

The present study is motivated by the recent publication[9,10] of experimental evidence obtained in interactions with strengths far greater than those employed to develop the preceding flowfield model. Significant features, which do not fit into the sequence presented in Ref. 5, are observed in the experimental surface flow visualization. These new features, and their impact on the mean flow off the surface, are crucial in the effort to understand details of high-speed compression. It is the purpose of the present work 1) to reproduce the observed surface features of Ref. 9 through numerical techniques, 2) to propose a computation-based three-dimensional flowfield structure corresponding to the observed surface features, and 3) to extend the evolution sequence of Ref. 5 to assimilate these new features.

Numerical Model

Governing Equations

The flowfield is assumed to be described by the three-dimensional mean compressible Navier–Stokes equations, which for numerical purposes are employed in strong conservation form. The effects of turbulence are accounted for by assuming an eddy viscosity and constant turbulent Prandtl number $Pr_t = 0.90$. The turbulence model used to determine the eddy viscosity is based on the k–ϵ equations[11,12] with low-Reynolds-number terms and a compressibility correction. The full equation set is documented in Ref. 13.

The governing equations are solved using the Roe flux-difference split scheme for the inviscid fluxes and standard second-order centered differencing for the viscous fluxes. An implicit time-integration scheme, based on the Beam–Warming approach,[14] is employed to march the solution to steady state. A partial consequence of the choice of governing equations, specifically their averaged nature—coupled with the lack of resolution of extremely small timescales and turbulence model uncertainties, is that the computations do not reproduce the inherent unsteadiness observed in such flows. Therefore, the results described next are relevant to aspects of the computed mean flow.

Received 7 February 2000; revision received 30 January 2001; accepted for publication 23 February 2001.

*Research Aerospace Engineer, 2210 Eighth Street, Computational Sciences Branch, Air Vehicles Directorate. Senior Member AIAA.

†Senior Research Aerospace Engineer, Computational Sciences Branch, Air Vehicles Directorate. Associate Fellow AIAA.

Table 1 Parameters of the numerical domain

Fin angle	$IL \times JL \times KL$	Xm/δ	Ym/δ	Zm/δ	Xe/δ	T/δ	$\Delta n_y u^*/\nu_w$
18 deg	$153 \times 143 \times 103$	69.67	26.85	25.78	61.62	13.16	0.5
23 deg mesh 1	$91 \times 72 \times 52$	74.43	26.85	40.40	55.28	16.93	1.05
23 deg mesh 2	$181 \times 143 \times 103$	74.43	26.85	40.40	55.28	16.93	0.5
23 deg mesh 3	$229 \times 179 \times 129$	74.43	26.85	40.40	55.28	16.93	0.5

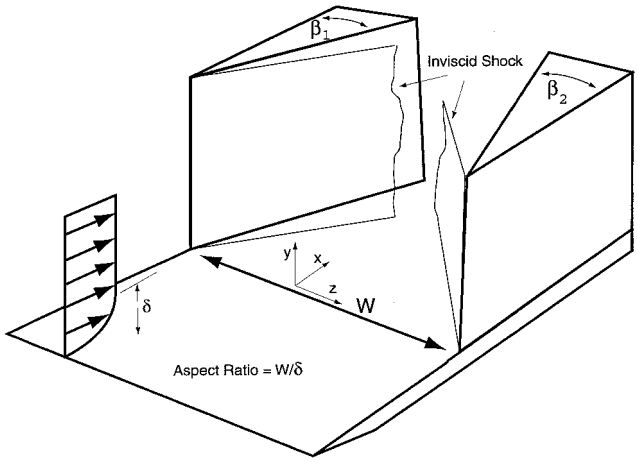

Fig. 1 Schematic of the double-fin generated crossing shock-wave/turbulent boundary-layer interaction.

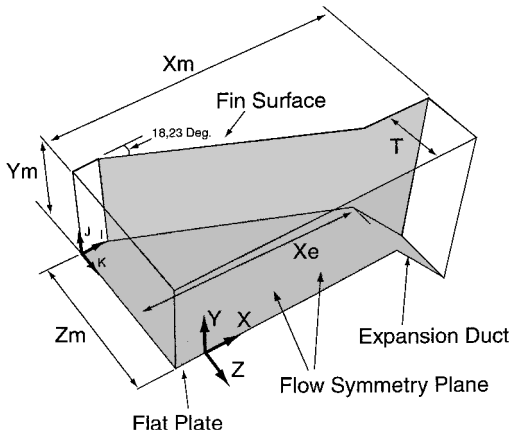

Fig. 2 Schematic of the computational domain.

Flow Conditions and Grid Geometry

The simulations model the recent experiments of Zheltovodov and Maksimov [9] and Schuelein and Zheltovodov.[10] The freestream Mach number and stagnation conditions are $M = 4.961$, $P_0 = 2.2$ Mpa, and $T_0 = 427$ K, respectively, resulting in a freestream unit Reynolds number of 36.5×10^6 per meter. The wall temperature is $T_w = 295$ K. Two symmetric double-fin configurations are examined, one with 18-deg fin angles, the other with 23-deg fin angles. In the experiment[9,10] the flat plate terminates prior to the trailing edges of the fins in both the 18- and 23-deg configurations. The free shear layer emanating from the downstream edge of the plate is difficult to simulate numerically, and its effects on the flow in the region of interest can be characterized as secondary. Therefore, the trailing region is modeled as an expansion by inserting a 45-deg downward ramp.

Because of the configuration symmetry, only half the domain is computed, as shown in Fig. 2. On the symmetry plane all gradients are set to zero with the exception of the normal velocity, which is itself set to zero instead. On the solid surfaces (flat plate, fins: shaded in Fig. 2) the no-slip boundary condition is invoked, with k, ϵ, and the normal pressure gradient specified to be zero. The inflow velocity profile is specified six boundary-layer thicknesses ($\delta = 3.8$ mm) upstream of the fin leading edge and is determined from separate two-dimensional calculations so that the momentum thickness of the incoming equilibrium boundary layer matches that reported in the experiment of Ref. 9 ($\theta = 0.157$ mm). At the outflow and top boundaries zero-gradient extrapolation boundary conditions are applied.

The grid employed for each simulation is composed of sequential nonuniform Cartesian planes oriented normal to the freestream direction. Grid points are clustered to resolve the secondary features of the interior vortical flowfield, with regions of increased resolution determined from previous experience. For the stronger, 23×23 deg interaction the solution is computed on several meshes with various grid spacings to establish the degree of mesh independence. The coarsest resolution mesh, mesh 1, consists of every other point in the medium resolution mesh, mesh 2, resulting in an effective doubling of the spatial resolution between the two meshes. Additional grid points are added in the interior regions of mesh 2 to yield the finest mesh, mesh 3, which has roughly twice as many points. A summary of the parameters for each mesh is presented in Table 1, where IL, JL, and KL represent the number of grid points in the streamwise, plate-normal, and spanwise directions, respectively, and the geometric quantities are marked in the schematic of the computational domain, Fig. 2. The grid spacing normal to the plate surface is listed in terms of wall units $y^+ = yu^*/\nu_w$, where u^* is the friction velocity, ν_w is the dynamic viscosity at the wall, and y is the distance from the wall. When evaluated using the conditions of the incoming equilibrium boundary layer, the grid spacing normal to the wall (Δn_y) for meshes 2 and 3 is less than one wall unit, as recommended for simulations with the k–ϵ model employed. Both meshes resolve the undisturbed incoming boundary layer with at least 50 points in the vertical direction. Convergence of the solution is determined from monitoring the global norm, surface pressure, and skin-friction coefficients.

Results

Comparison with Experiment

In Fig. 3 the spanwise surface pressure distributions for the 23×23 deg interaction are compared at several streamwise stations with the experimental data of Ref. 9. In each plot the distance from the fin leading edge is labeled, and the pressure P has been normalized by the freestream value P_∞. The abscissa is the distance from the interaction centerline normalized by the boundary-layer thickness $Z(\delta)$. At the anterior stations $X = 22.1$ and 24.7δ the pressure profile is similar to that of the well-documented single-fin interaction, and results from all three meshes exhibit close agreement with available experimental data. Farther downstream $X = 32.6\delta$, the pressure profile exhibits the impact of the shock system caused by the opposing fin. With the exception of regions near the location of the peak pressure—shown subsequently to correspond to flow attachment near the fin plate corner, the solutions are relatively well resolved.

Figure 4 depicts the spanwise pressure at several planes for the 18×18 deg interaction. In this case too the computations show overall good agreement with the experimental data in the major portion of the domain. Near the symmetry plane however, while the trends are reproduced, significant quantitative discrepancies are evident for both geometries. Although both experiment and computations exhibit a rapid rise in pressure on approaching $Z \sim 0$, the computational values are substantially higher. Numerical experiments in which the Roe flux-difference split scheme was replaced with a standard centered difference with damping method[15] yield nearly identical trends. Similarly, length scale[16] and turbulence kinetic energy limiting models[17] fail to improve the quantitative comparison. Although the source of the discrepancy is unclear, the anomaly on the centerline may be the result of the failure of the turbulence model,

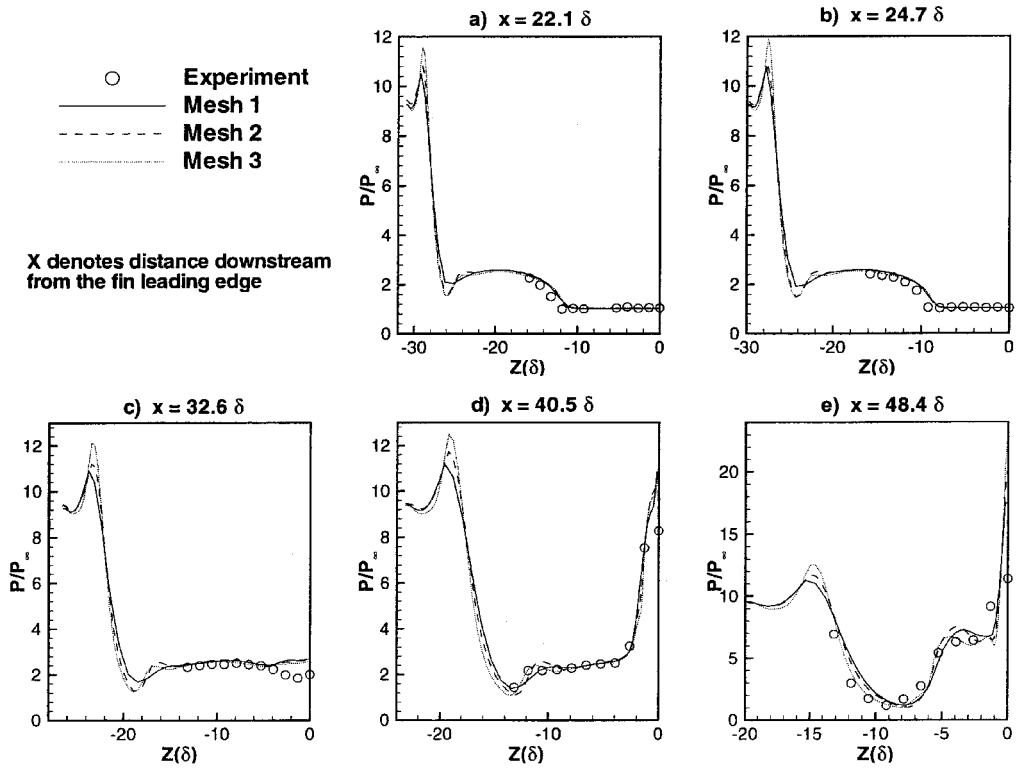

Fig. 3 Surface pressure distributions in the 23 × 23 deg interaction.

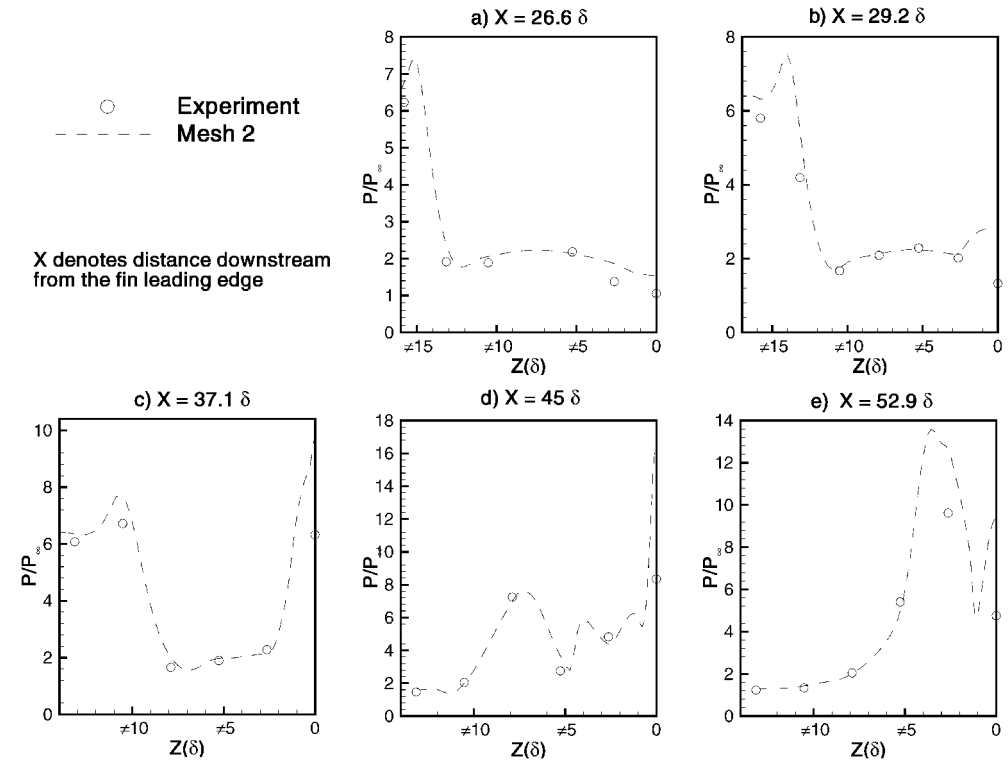

Fig. 4 Surface pressure distributions in the 18 × 18 deg interaction.

extrapolated from two-dimensional experience, to treat the complex three-dimensional structure represented by the centerline vortex. A similar situation was observed in Ref. 18 with regard to skin-friction coefficients on the centerline of the interaction and more recently for heat-transfer coefficients.[19] The appearance of the discrepancies in the pressure distributions in the current effort, a quantity predicted reasonably accurately in earlier studies, can result from the significantly stronger interactions examined.

There is substantial evidence that the computations reproduce the mean flowfield very accurately. This statement is based on the fact that in previous efforts on weaker, but nonetheless fully separated, interactions computations have faithfully reproduced a variety of experimental results, including surface oil flow patterns, shock structure, and pitot surveys.[4,20] As shown next, in the present extremely strong interactions, the available evidence suggests that this continues to be the case.

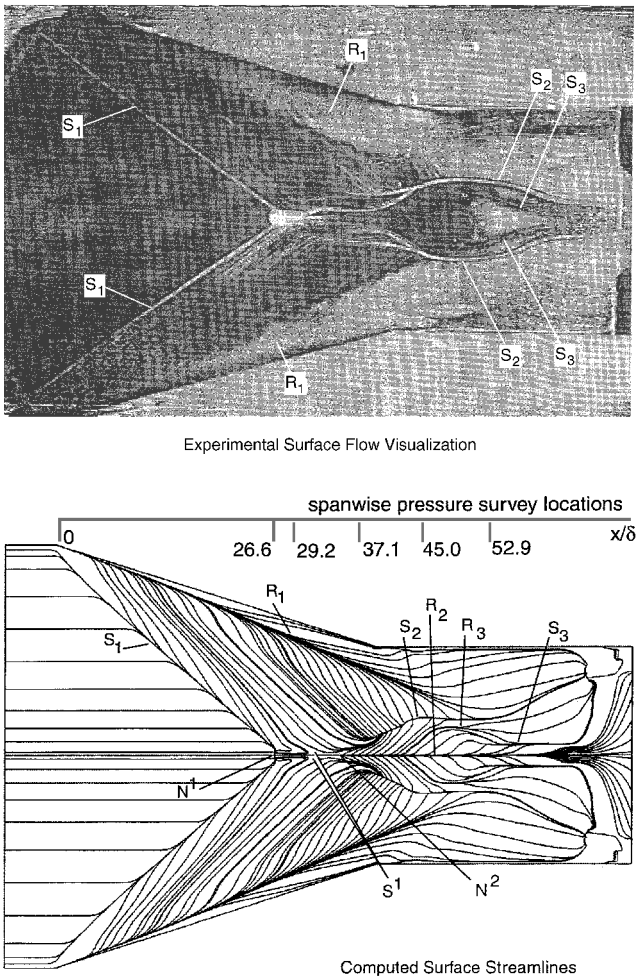

Fig. 5 Surface streamline topology in the 18 × 18 deg interaction.

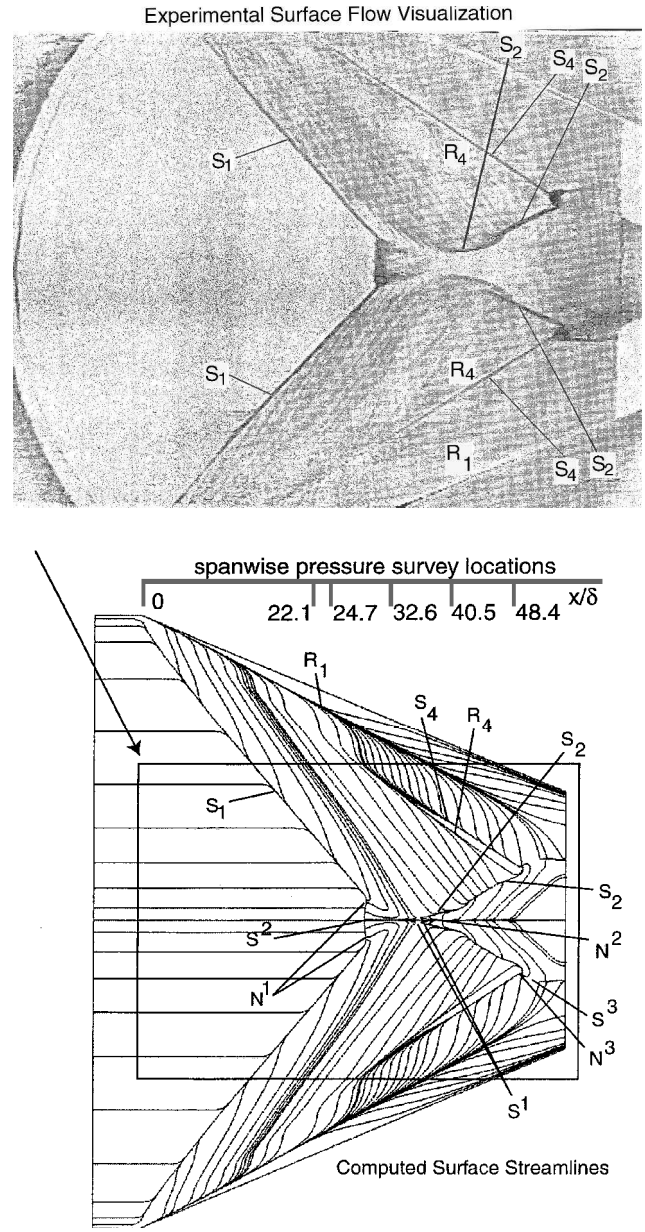

Fig. 6 Surface streamline topology in the 23 × 23 deg interaction.

Figures 5 and 6 depict both the experimentally inferred and computed surface streamlines for the 18 × 18 and 23 × 23 deg interactions. Because the computed surface streamlines were essentially invariant for the simulations on meshes 2 and 3, only results on the former are shown. In the subsequent discussion the expression "surface oil" or "surface streamline" pattern (or flow), when employed in the context of computations, denotes the method of reproducing the results of experimental surface flow visualization by releasing particles at the first mesh point away from the surface and following their trajectory under the assumption that the plate-normal velocity is zero. An equivalent method of utilizing the surface skin-friction vector yields nearly identical results. Although lines of separation and attachment have numerical designators subscripted, critical points have their designators superscripted; this serves to distinguish between saddles and lines of separation. Additionally, because of the symmetry of the interaction, identical features on either side of the interaction centerline bear the same label. This notation is chosen to facilitate a consistent nomenclature and is a departure from that employed in the experiments of Ref. 9.

Although the present Mach 5 18 × 18 deg interaction is much stronger than the Mach 4 15 × 15 deg configuration examined in Ref. 20, the dominant surface oil flow features are generally similar. Lines of coalescence S_1, representing primary separation, and divergence R_1, denoting primary attachment are formed as a result of the swept interaction of each fin. Downstream, the two primary lines of separation evolve into a complex structure yielding a centerline of attachment R_2 straddled by two lines of separation S_2. As shown in Ref. 20, these separation lines and corresponding centerline vortices occur in conjunction with the impingement of the two distinct entrainment flows caused by each fin. Farther downstream, additional features are evident, marked in the experimental oil flow as S_3. The numerical result not only exhibits these features but also shows corresponding attachment lines R_3, which are required for consistency. The critical points observed in Fig. 5 are precisely the same as those reported in Ref. 5 for the Mach 4 15 × 15 case: four critical points arranged in a diamond-shaped pattern with two nodes N^1 and N^2 on the interaction centerline and a pair of saddles S^1 and its mirror image, on either side of the centerline between the nodes. Hence, from the standpoint of number and types of critical points, the Mach 5 18 × 18 case is identical to the Mach 4 15 × 15 case described in Ref. 20.

Several new and significant features appear in the experimental data for the much stronger 23 × 23 deg interaction (Fig. 6), each of which is reproduced accurately by the computation. The primary lines of separation and attachment remain S_1 and R_1, respectively. The downstream structure consisting of two lines of separation S_2 on either side of the centerline attachment is also maintained, although the features S_3 and R_3 are not seen because of the limited downstream extent of the geometry. A new separation line S_4 is evident, aligned along an angle approximately between the primary separation and attachment lines. There is a clearly identifiable attachment line R_4 in its close vicinity. The separation associated with S_4–R_4 pair has been referred to as secondary separation in earlier studies of the single-fin interaction. A new critical point configuration is also

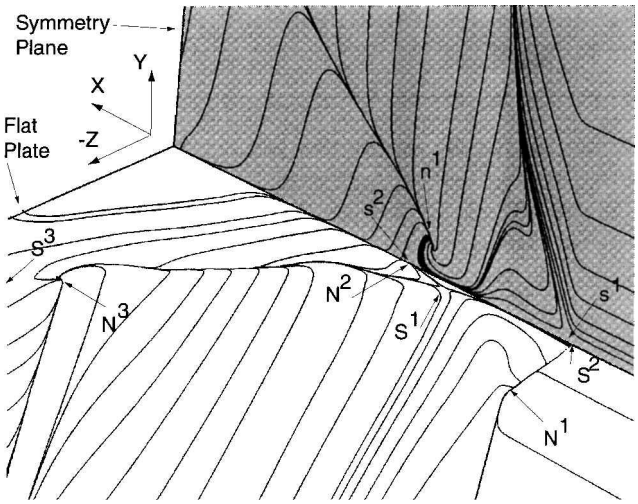

Fig. 7 Surface streamlines near the centerline in the 23 × 23 deg interaction.

observed in the 23 × 23 deg surface map. The centerline node N^1 can be considered to have bifurcated into the saddle-node S^2–N^1 combination, the saddle being located on the centerline and the two nodes N^1 off centerline on either side. Downstream, S_4 and S_2 terminate in a node-saddle (N^3–S^3) combination. In concluding this section it is noted that the rule governing critical points requiring equality of nodes and saddles is satisfied under this new configuration.

Analysis of the Computations

Surface Streamline Topology

Because the surface pattern of the 18 × 18 deg interaction is generally similar to that reported in earlier efforts,[3] it is not discussed in detail. The principal new features are the appearance of tertiary separation and attachment features in the form of R_3 and S_3 (Fig. 5).

As noted earlier, the surface flow pattern shown in Fig. 6 for the stronger 23 × 23 deg interaction is substantially different from that observed in Fig. 5. This new topological configuration indicates the onset of a new flow regime for this very strong interaction. To investigate further, a more detailed view of the kinematic structure is shown in Fig. 7. Also shown are select streamlines in the symmetry plane normal to the plate. These streamlines can be interpreted as intersections of stream surfaces with the symmetry plane. Critical points on the symmetry plane are designated by lowercase letters. The streamline structure on the symmetry plane exhibits the presence of two half-saddles at the surface s^1 and s^2 and a focus/node above the surface n^1, similar to those in earlier interactions reported in Ref. 5. This new development is similar to the owl-face type of pattern discussed in Ref. 21.

On the plate surface the two primary lines of coalescence each terminate into off-centerline foci (N^1 and its mirror counterpart) rather than in the single node on the centerline as in Fig. 5. The same designation N^1 is employed for the foci in both Figs. 5 and 6 because we take the point of view that the new topology of Fig. 6 is an evolved version of that reported in Ref. 5 (and shown in Fig. 5). A new saddle-point S^2 is observed on the centerline and is linked to each of the foci N^1 through lines of coalescence. Although there is a clear distinction between these lines on the one hand and the primary lines of separation S_1 on the other, they are separated by a node N^1—at present separate designators are not employed. It is evident that the topological bifurcation of Fig. 6 represents a fundamental departure from the simpler model of Ref. 5. The pattern in the symmetry plane is qualitatively the same as that reported in Ref. 3. The fact that the symmetry plane pattern has remained unaltered despite the modification in surface pattern reiterates the lack of a one-to-one relationship between the observed surface pattern and the off-surface flowfield. In Fig. 8 the new topological regime has been added in schematic form to the previously reported succession[5] of observed configurations with increasing interaction strength. Figure 8a depicts the schematic in the limit of complete absence of interaction, i.e., when the fin angles are both zero. In this case both the surface and symmetry plane lines are undisturbed. As the interaction strength is increased, various lines of coalescence and divergence form on the surface. Simultaneously, in the symmetry plane the fluid in the incoming boundary layer moves away from the surface. Figures 8c–8e display the sequence of bifurcations observed as the interaction strength is increased. In Fig. 8e the diamond-shaped pattern of Fig. 5 is observed. Finally, in Fig. 8f the bifurcation of the upstream node into the saddle-twin node configuration observed in Fig. 7 is shown.

The final major critical point manifestation occurs downstream where a focus-saddle combination N^3–S^3 is observed. The focus is stable in that neighboring surface streamlines approach the critical point. This pattern typically represents the presence of a vortex filament emanating from the surface into the flow. The kinematic impact of this pattern on the flowfield structure is described next. The downstream node-saddle pair N^3 and S^3 has not been incorporated in Fig. 8 because the figure emphasizes aspects of flow development near the symmetry plane.

Three-Dimensional Structure

The preceding method of describing a three-dimensional separated flowfield emphasized topological aspects of the field. The approach has the advantage of introducing an element of rigor into the description. However, considerable additional insight into the three-dimensional structure of the flow can be obtained through analysis of paths of theoretical particles released in the flowfield as was performed in previous efforts.[20] By joining the paths of carefully selected particles into ribbons identifying stream surfaces (ribbon plots), coherent regimes can be defined to clearly describe the complex flowfield.

Ribbon plots revealing the flowfield structure for the 18 × 18 and 23 × 23 deg interactions are plotted in Figs. 9a and 9c. The computed surface streamlines for each interaction are plotted beneath the corresponding ribbon plots. With the exception of features associated with tertiary separation S_3 and attachment R_3, the flowfield structure in the 18 × 18 deg interaction is generally similar to that shown in Ref. 5. The incoming boundary layer separates along the primary separation line and does not reattach. The fluid from the upstream boundary layer instead forms the separated boundary-layer regime, a region of low energy flow above the rest of the interaction. The vortex interaction region contains the fluid that attaches near the fin and sweeps spanwise to fill the void left by the separated boundary-layer fluid. Some of the fluid in the vortex interaction region separates on the downstream side of the primary separation line. The vortex interaction regime comprises a significant portion of the primary vortex in the single-fin interaction. Fluid originating near the fin leading edge, which is swept spanwise to the symmetry plane before turning downstream, comprises the centerline vortex region. Finally, high-energy fluid from the inviscid region near the fin leading edge, the entrainment flow regime, attaches downstream and sweeps toward the interaction centerline before separating. The distinct footprint of each regime is shown in the surface streamline plot located beneath the ribbon plot in Fig. 9b. As noted earlier, the new lines of coalescence on the surface R_3 and S_3 represent tertiary attachment and separation. The features associated with these surface features have not been examined in the present work.

The preceding four regimes can again be identified in the stronger 23 × 23 deg interaction from inspection of the ribbon and surface streamline plots shown in Figs. 9c and 9d. However, a complete description requires the introduction of several new regimes. The separated boundary layer and vortex interaction regimes separate on either side of the primary separation line, but near the interaction centerline two vortex filaments (only one shown) leave the surface at the two foci on either side of the interaction centerline. In a simplistic sense the separated boundary-layer sheet forms kinks caused by the vortex filaments associated with the node N^1 and its mirror image. The centerline vortex region in the 23 × 23 deg interaction shows generally similar behavior to that seen in the weaker interaction. Separation identified with S_2 in Fig. 5 and its equivalent in Fig. 6 is associated with a shock feature, which can be traced to the system originating from the opposite fin. This shock precipitates separation of the entrained regime as it essentially impinges on the symmetry

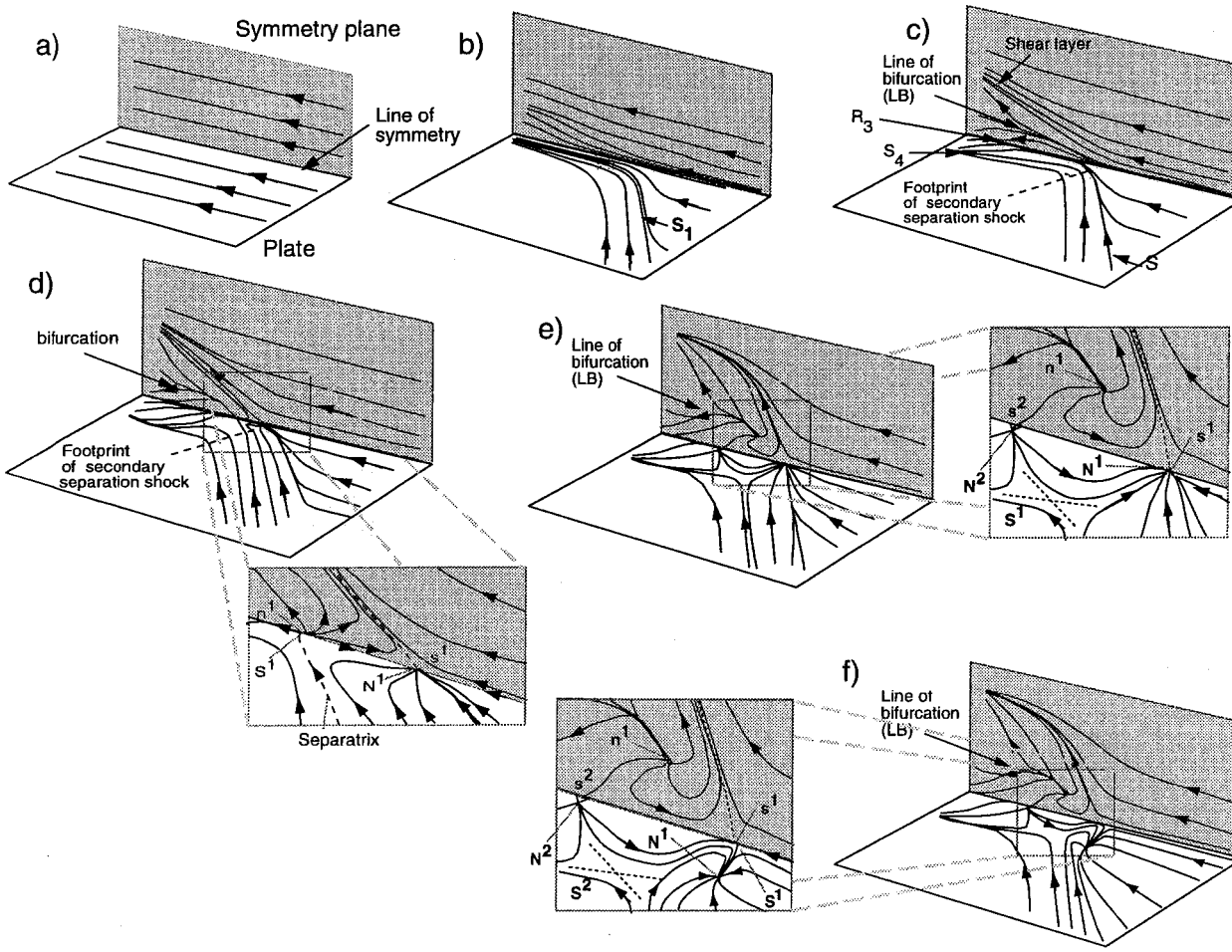

Fig. 8 Observed evolution of the computed separation topology with increase in interaction strength.

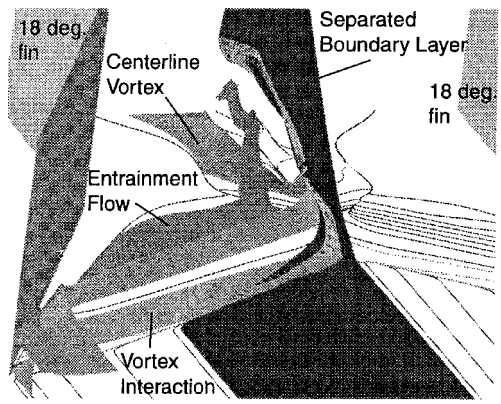

Fig. 9a Ribbon plot for 18 × 18 deg interaction.

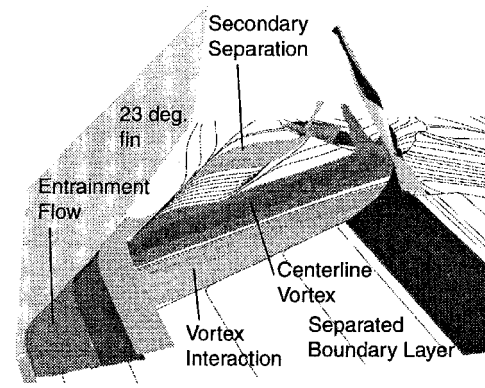

Fig. 9c Ribbon plot for 23 × 23 deg interaction.

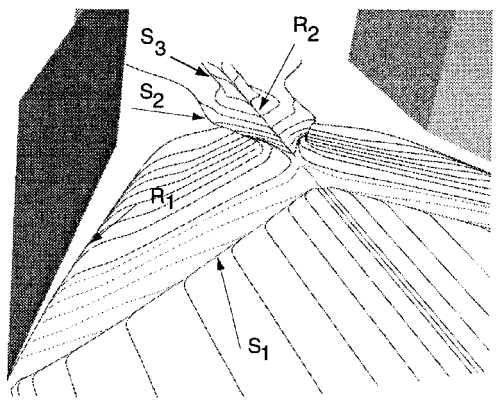

Fig. 9b Surface streamlines for 18 × 18 deg interaction.

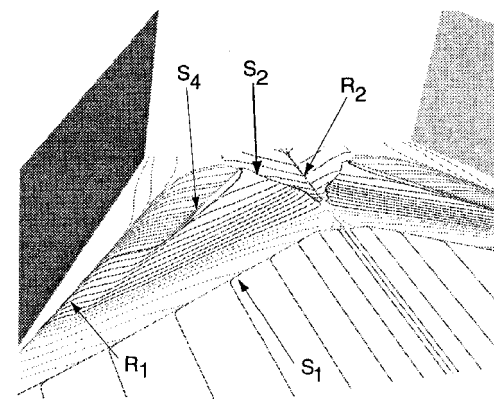

Fig. 9d Surface streamlines for 23 × 23 deg interaction.

plane after formation of a wall-jet-like structure. When secondary separation is present, as in Fig. 6, the wall-jet-like flow between R_4 and S_2 is only marginally developed after attachment at R_4 and can thus yield the observed difference in orientation between S_2 in Fig. 5 and S_2 in Fig. 6. The entrainment flow region is similar to that observed in the weaker interactions, but with a limited spanwise range as a result of the appearance of secondary separation.

The final aspect examined is that of secondary separation (S_4–R_4 pair) and the associated critical points N^3 and S^3, respectively. Although commonly observed in delta-wing flows, the phenomenon is relatively rare in shock/turbulent boundary-layer interactions. It has previously been reported in experimental observations of the single-fin configuration in strong interactions,[22,23] and evidence suggests that the phenomenon occurs only in a narrow range of interaction parameters.[2] This regime is marked in the stream ribbons and surface patterns of Figs. 9c and 9d. The secondary separation lines terminate at the downstream foci where a second pair of vortex filaments leave the surface.

As reported in the earlier experimental work of Refs. 22 and 23, the secondary separation observed in the 23 × 23 deg interaction has been observed in the flowfield generated by a single fin. The feature has been reproduced computationally in single-fin interactions in Ref. 24 through an elegant modification to the Baldwin–Lomax model. In the present work the baseline k–ϵ model was not modified in any specific manner to obtain the observed details. Secondary separation was not observed on the coarsest mesh as a result of insufficient grid resolution. The spanwise structure of the pressure gradient in the interaction, determined by plotting the magnitude of the three-dimensional pressure gradient vector field $|\nabla P|$, is shown in Fig. 10 superimposed above the surface flow. From inspection of Fig. 10, it can be seen that a local region of strong pressure gradients, indicative of a shock wave, appears above the secondary separation line. The presence of this local shock wave is detected in the spanwise wall pressure distributions (Fig. 3) as the small peak near the end of the plateau region as the fin surface is approached. This local pressure peak is not observed in the spanwise pressure distributions for the 18 × 18 deg interaction where secondary separation does not occur. Alvi and Settles[22] report the appearance of shock waves in the flow beneath the lambda-structure in their experimental study of strong single-fin interactions where secondary separation has occurred.

A final comment is made regarding the shock structure in the 23 × 23 deg interaction. Many of the dominant features observed in earlier efforts on the Mach 4 15 × 15 deg interaction[20] persist in the 23 × 23 deg interaction. However, some new features are evident, which will be discussed in detail in a subsequent publication. One such new development is briefly mentioned here because it suggests that this is among the strongest cases for which a mean steady flow can be obtained. Figures 11 and 12 show the shock structure, plotted again with the magnitude of the three-dimensional pressure gradient, at the top boundary plane. It is evident that the primary shocks cross each other in a regular fashion for the 18 × 18 deg interaction but

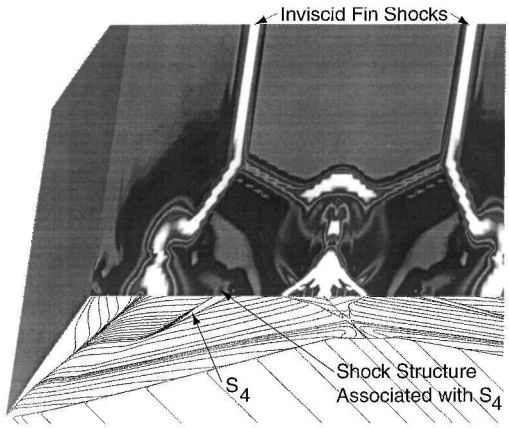

Fig. 10 Surface streamline structure and magnitude of the pressure gradient for the 23 × 23 deg interaction.

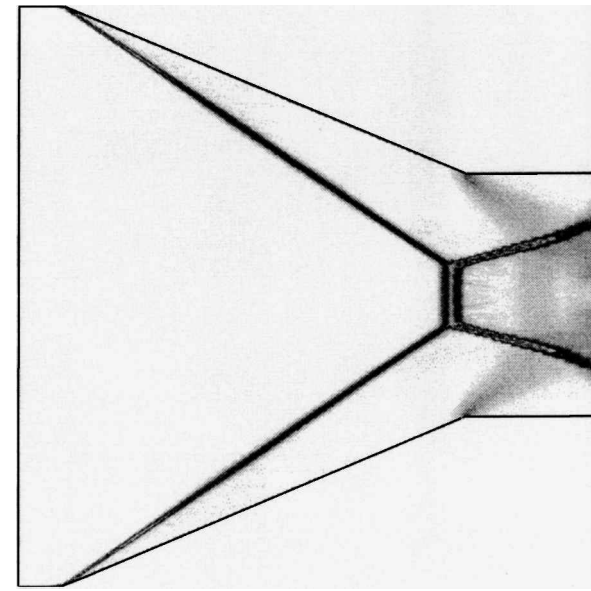

Fig. 11 Shock-wave structure in the 23 × 23 deg interaction.

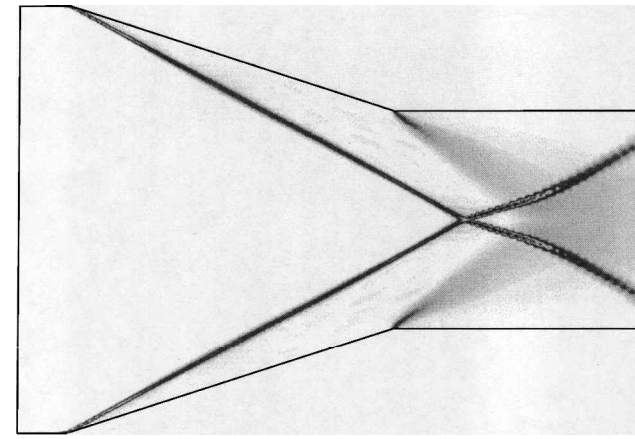

Fig. 12 Shock-wave structure in the 18 × 18 deg interaction.

form a Mach stem or irregular crossing in the 23 × 23 deg case. The appearance of the Mach stem is not entirely unexpected because, for a freestream Mach number of 5, the oblique shock wave resulting from the 23 deg deflection angle is in the dual-solution domain,[25] where both regular and irregular shock reflections are theoretically possible. To date, experimental investigation of the transition from regular to Mach reflection in the dual-solution domain[26–28] has indicated that the transition occurs at the Neumann condition,[25] which corresponds to a flow deflection angle of 20.87 deg at Mach 5. Although the flow is subsonic immediately downstream of the Mach stem, the expansion duct (see Fig. 2) ensures supersonic outflow at most locations on the downstream boundary. Because the two-dimensional inviscid flow permits the existence of a regular crossing solution, confirmed analytically and with separate two-dimensional computations, several numerical experiments were conducted to seek such a regular pattern as an asymptote of the present flow by raising the height of the computed domain. In each of these cases, however, no effect was observed on the irregular reflection phenomenon. This aspect needs further investigation, including evaluation of possible hysteresis.[25] A coupled effect concerns three-dimensionality: small perturbations, even if introduced in the initial transients, can influence the final observed shock-crossing pattern particularly if the flow parameters lie near a bifurcation boundary.

Conclusions

The numerical simulation of the 18 × 18 and 23 × 23 deg Mach 5 crossing shock-wave/turbulent-boundary-layer interactions has revealed the existence of new structures in the stronger 23 × 23

deg interaction. Although the computed surface pressures exhibit generally close agreement with the surface pressures obtained from experiment, the computed surface streamlines reproduce the experimental inference with remarkable fidelity. Noteworthy observations from the numerical study include the following:

1) The critical point topology and dominant aspects of the three-dimensional structure of the Mach 5 18×18 deg interaction are qualitatively the same as those observed in earlier studies of the Mach 4 15×15 deg configuration.

2) The stronger Mach 5 23×23 deg interaction exhibits a new critical point topology. The upstream centerline nodal point, observed in the weaker interactions, bifurcates into a centerline saddle point with a pair of foci on either side. Much farther downstream a new node/saddle pair is observed in conjunction with secondary separation and attachment in the classic sense of single-fin interactions.

Acknowledgments

The authors are grateful for Air Force Office of Scientific Research sponsorship under tasks monitored by R. Canfield, W. Hilbun, and S. Walker. The experimental observations were provided by A. Zheltovodov. The authors acknowledge several insightful communications with A. Zheltovodov and M. Visbal. This work was also supported in part by a grant of High-Performance Computing (HPC) time from the U.S. Department of Defense HPC Shared Resource Centers at the U.S. Army Engineer Research and Development Center and the Naval Oceanographic Office.

References

[1]Panaras, A. G., "Review of the Physics of Swept-Shock/Boundary Layer Interactions," *Progress in Aerospace Science*, Vol. 31, 1995, pp. 173–244.

[2]Settles, G. S., and Dolling, D. S., "Swept Shock-Wave/Boundary-Layer Interactions," *Tactical Missile Aerodynamics: General Topics*, edited by M. J. Hemsch, Vol. 141, Progress in Astronautics and Aeronautics, AIAA, Washington, DC, 1992, pp. 297–379.

[3]Gaitonde, D., Shang, J. S., and Visbal, M. R., "Structure of a Double-Fin Turbulent Interaction at High Speed," *AIAA Journal*, Vol. 33, No. 2, 1995, pp. 193–200.

[4]Gaitonde, D. V., and Shang, J. S., "On 3-D Shock-Wave/Turbulent Boundary Layer Interactions at Mach 4," AIAA Paper 96-0043, Jan. 1996.

[5]Gaitonde, D., Shang, J. S., Garrison, T. J., Zheltovodov, A. A., and Maksimov, A. I., "Evolution of the Separated Flowfield in a 3-D Shock Wave/Turbulent Boundary Layer Interaction," AIAA Paper 97-1837, June 1997.

[6]Gaitonde, D., Shang, J. S., Garrison, T. J., Zheltovodov, A. A., and Maksimov, A. I., "Three-Dimensional Turbulent Interactions Caused by Asymmetric Crossing-Shock Configurations," *AIAA Journal*, Vol. 37, No. 12, 1999, pp. 1602–1608.

[7]Gaitonde, D., and Shang, J. S., "The Structure of a Double-Fin Turbulent Interaction at Mach 4," AIAA Paper 94-2810, June 1994.

[8]Chapman, G. T., and Yates, L. A., "Topology of Flow Separation on Three-Dimensional Bodies," *Applied Mechanics Reviews*, Vol. 44, No. 7, 1991, pp. 329–345.

[9]Zheltovodov, A. A., and Maksimov, A. I., "Hypersonic Crossing-Shock-Waves/Turbulent Boundary Layer Interactions," Russian Academy of Sciences, TR Final Rept., EOARD Contract F61775-98-WE091, Novosibirsk, Russia, April 1999.

[10]Schuelein, E., and Zheltovodov, A. A., "Development of Experimental Methods for the Hypersonic Flows Studies in Ludwieg Tube," *Proceedings of the International Conference on the Methods of Aerophysical Research: Part 1*, Inst. of Theoretical and Applied Mechanics, Novosibirsk, Russia, 1998, pp. 191–199.

[11]Jones, W. P., and Launder, B. E., "The Prediction of Laminarization with a Two-Equation Model of Turbulence," *International Journal of Heat and Mass Transfer*, Vol. 15, No. 2, 1972, pp. 301–314.

[12]Launder, B. E., and Sharma, B. I., "Application of the Energy Dissipation Model of Turbulence to the Calculation of Flows near a Spinning Disk," *Letters in Heat and Mass Transfer*, Vol. 1, 1974, pp. 131–138.

[13]Rizzetta, D. P., "Numerical Simulation of Turbulent Cylinder Juncture Flowfields," AIAA Paper 93-3038, July 1993.

[14]Beam, R., and Warming, R., "An Implicit Factored Scheme for the Compressible Navier–Stokes Equations," *AIAA Journal*, Vol. 16, No. 4, 1978, pp. 393–402.

[15]Jameson, A., Schmidt, W., and Turkel, E., "Numerical Solutions of the Euler Equations by a Finite Volume Method Using Runge–Kutta Time Stepping Schemes," AIAA Paper 81-1259, June 1981.

[16]Rodi, W., "Experience with Two-Layer Models Combining the k–ϵ Model with a One-Equation Model near the Wall," AIAA Paper 91-0216, Jan. 1991.

[17]Menter, F. R., "Zonal Two Equation k–w Turbulence Models for Aerodynamic Flows," AIAA Paper 93-2906, July 1993.

[18]Gaitonde, D., and Shang, J. S., "Skin-Friction Predictions in a Crossing-Shock Turbulent Interaction," *Journal of Propulsion and Power*, Vol. 13, No. 3, 1997, pp. 342–348.

[19]Thivet, F., Knight, D. D., Zheltovodov, A. A., and Maksimov, A. I., "Some Insights in Turbulence Modeling for Crossing-Shock-Wave/Boundary-Layer Interactions," AIAA Paper 2000-0131, Jan. 2000.

[20]Gaitonde, D., and Shang, J. S., "Structure of a Double-Fin Interaction at Mach 4," *AIAA Journal*, Vol. 33, No. 12, 1995, pp. 2250–2258.

[21]Perry, A. E., and Chong, M. S., "A Description of Eddying Motions and Flow Patterns Using Critical-Point Concepts," *Annual Review of Fluid Mechanics*, Vol. 19, 1987, pp. 129–155.

[22]Alvi, F. S., and Settles, G. S., "Physical Model of the Swept Shock Wave/Boundary-Layer Interaction Flowfield," *AIAA Journal*, Vol. 30, No. 9, 1992, pp. 2252–2258.

[23]Zheltovodov, A. A., Maksimov, A. I., and Shilein, E. K., "Development of Turbulent Separated Flows in the Vicinity of Swept Shock Waves," *The Interactions of Complex 3-D Flows*, edited by A. M. Kharitonov, Inst. of Theoretical and Applied Mechanics, USSR Academy of Sciences, Novosibirsk, Russia, 1987, pp. 67–91.

[24]Panaras, A. G., "Algebraic Turbulence Modeling for Swept Shock-Wave/Turbulent Boundary-Layer Interactions," *AIAA Journal*, Vol.35, No. 3, 1997, pp. 456–463.

[25]Hornung, H., "Regular and Mach Reflection of Shock Waves," *Annual Review of Fluid Mechanics*, Vol. 18, 1986, pp. 33–58.

[26]Skews, B. W., "Three-Dimensional Effects in Wind Tunnel Studies of Shock Wave Reflection," *Journal of Fluid Mechanics*, Vol. 407, 2000, pp. 85–104.

[27]Ivanov, M. S., Kharitonov, A. M., Khotyanovsky, D. V., Kudryavtsev, A. N., Markelov, G. N., and Nikiforov, S. B., "Numerical and Experimental Study of 3D Steady Shock Wave Interactions," AIAA Paper 2001-0740, Jan. 2001.

[28]Hornung, H. G., and Robinson, M. L., "Transition from Regular to Mach Reflection of Shock Waves Part 2. The Steady-Flow Criterion," *Journal of Fluid Mechanics*, Vol. 123, 1982, pp. 155–164.

M. Sichel
Associate Editor